

Physical properties of Zn doped Fe₃O₄ nanoparticles

G. SOUCA^{a,*}, R. DUDRIC^a, C. IACOVITA^b, A. MOLDOVAN^c, T. FRENTIU^d, R. STIUFIUC^{b,c}, C. M. LUCACIU^b, R. TETEAN^a, E. BURZO^a

^aFaculty of Physics, "Babes Bolyai" University, Kogalniceanu 1, 400084 Cluj-Napoca, Romania

^bDepartment of Pharmaceutical Physics-Biophysics, Faculty of Pharmacy, "Iuliu Hatieganu" University of Medicine and Pharmacy, Pasteur 6, 400349 Cluj-Napoca, Romania

^cDepartment of Bionanoscopia, MedFuture Research Center for Advance Medicine, "Iuliu Hatieganu" University of Medicine and Pharmacy, Pasteur 4-6, 400337 Cluj-Napoca, Romania

^dFaculty of Chemistry and Chemical Engineering, "Babes Bolyai" University, 11 Arany Janos, 400028, Cluj-Napoca, Romania

Two series of octahedral Fe_{3-x}Zn_xO₄ nanoparticles with mean sizes of 27 nm and 73 nm were prepared by thermal decomposition. All samples crystallize in inverse spinel cubic type structure with the Zn²⁺ ions located in tetrahedral sites. Magnetic measurements indicate an increase of the saturation magnetizations by 20% for a Zn content of x=0.12. The estimated anisotropy constants are close to that of pure magnetite. The physical properties of the investigated series are analysed in correlation with their structural properties.

(Received January 13, 2020; accepted June 16, 2020)

Keywords: Fe_{3-x}Zn_xO₄ nanoparticles, Crystal structure, Magnetic properties

1. Introduction

The applications of bio-functionalized magnetite nanoparticles for the vitro diagnostic represent an important field of research due to their biocompatibility and easy removal from the body by natural routes [1]. The magnetite nanoparticles can be also efficiently stabilized in corrosive biological media, by SiO₂ and Au coating, ensuring plasmonic properties. However, by coating the magnetite nanoparticles with nonmagnetic shells, their magnetic moments per volume unit decrease. It is thus of interest to investigate the behaviour of magnetite-based nanoparticles where the increase of magnetization can be obtained by iron substitutions. In this context, we report the preparation and physical properties of Fe_{3-x}Zn_xO₄ nanoparticles that have a reduced toxicity in comparison with other ferrites [2].

The magnetite (Fe³⁺)_A(Fe³⁺Fe²⁺)_B crystallizes in a cubic inverse spinel structure, space group *Fd3m*, with the lattice parameter *a* = 0.8397 nm. The tetrahedral (A) sites are occupied by ferric ions, while in the octahedral (B) sites both ferrous and ferric ions are located. The magnetite is ferrimagnetically ordered, the iron moments in octahedral and tetrahedral sites respectively, being antiparallely oriented.

The location of Zn²⁺ ions in the magnetite structure, as well as the magnetic properties of this system were found to depend significantly on the synthesis and/or postprocessing method [3 - 12]. Several reports suggested that a small number of Zn²⁺ ions would occupy octahedral sites, when Fe_{3-x}Zn_xO₄ was prepared by coprecipitation [4], ball-milling [5, 6], twin roller grinding methods [7], sputtering [8] or pulsed laser deposition [9]. The Zn²⁺ ions

dominantly occupy the tetrahedral sites when samples are obtained by thermal decomposition, thus inducing metastable Fe_{3-x}Zn_xO₄ phases with disordered arrangements of Zn²⁺ and Fe³⁺ ions [3, 10 - 12].

In the following, the physical properties of Zn doped magnetite nanoparticles having octahedral shapes, obtained by thermal decomposition method, are reported. The present data confirm the location of Zn²⁺ ions in tetrahedral sites.

2. Experimental

2.1. Nanoparticles synthesis

The Zn doped nanoparticles were obtained from mixtures of 0.7 mmol iron (III) acetylacetonate Fe(acac)₃, 1.05 mmol Zn (II) acetylacetonate (sample S1) or 1.0 mmol Fe (acac)₃, 1.5 mmol Zn (acac)₂ (sample S2), with 3.78 mmol oleic acid and 52.61 mmol benzylether. The above mixtures were heated up to T = 295° C with a rate of 5° C/min, kept at this temperature 30 min and cooled down to the ambient temperature. The Zn-doped nanoparticles were magnetically separated from the mixture and washed several times with ethylic alcohol. The samples were kept in ethylic alcohol before measurements.

2.2. Characterization

The SPECTRO CIROSCCD spectrometer (Spectro, Kleve, Germany) was used for the determination of Fe and Zn (n=3 measurements) by ICP-OES. The samples are

subjected to microwave-assisted digestion using Berghof MWS3+ (Berghof, Germany) high-pressure microwave digestion system in PTFE closed vessels, using 9 mL HCl 37% and 3 mL HNO₃ 69%. The digest was transferred to a volumetric flask, made up to 25 mL with double distilled water, filtered and stored in polyethylene flask until analysis. Determination was based on external calibration using a 8-point linear calibration curve over the range 0 – 10 mg/l element in 2% HNO₃.

The shape and sizes of Zn-doped magnetite nanoparticles were analysed by TEM using a Hitachi HT700 microscope equipped with an 8-megapixel CCD camera, operating at 100 keV in high contrast. X-ray diffraction measurements were carried out at ambient temperature using a Bruker D8 Advance Bruker Diffractometer with CuK_α radiation. The lattice parameters were determined using FullProf software [13].

Magnetic measurements were performed in the temperature range 5 K ≤ T ≤ 310 K by using a Vibrating Sample Magnetometer from Cryogenics, in fields up to μ₀H = 12 T and with a Faraday-type balance in external field up to μ₀H = 1 T in the temperature range 300 K ≤ T ≤ 850 K. The ZFC results were obtained in a field of μ₀H = 0.05 T after cooling at T = 5 K in the absence of external

fields. The FC measurements were recorded in the same field, after cooling the samples in the presence of an external field of 0.05 T.

3. Results

The TEM images of Fe_{3-x}Zn_xO₄ samples evidenced mainly the presence of faceted nanoparticles (Fig 1). Previously [14], was shown that the octahedral shapes of magnetite nanoparticles can be obtained by heating at T = 200° C with rates higher than 5° C/min, while spherical nanoparticles are formed at lower heating rates. Thus, the obtained octahedral shapes of Fe_{3-x}Zn_xO₄ nanoparticles can be correlated with a rather high temperature used for thermal treatment, as well as a relatively high heating rate. As a result, the nuclei formation rate and the growth process are rather high, favouring the formation of the {111}, facets with smaller surface energy compared to those of {011} or {101} planes. The octahedral particle shapes have a reduced surface energy, the flat surfaces of the octahedra possessing a small number of broken bonds and oxygen vacancies.

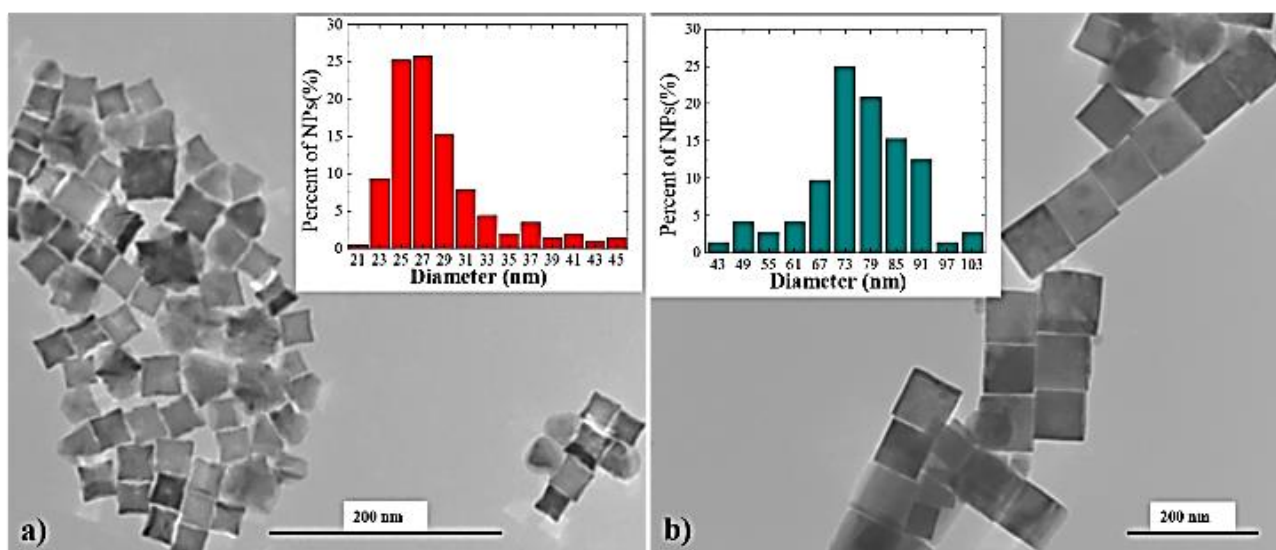


Fig. 1 TEM patterns of samples S1 (a) and S2 (b). In inset are given the particle sizes distribution (color online)

The size distributions for S1 and S2 nanoparticle series, determined by TEM, are given in the insets of Fig.1. For S1 samples, the greatest fraction of nanoparticles is situated between 22 nm and 30 nm with a mean size of 27 nm. Higher dimensions are evidenced in S2 samples, their mean value being of ≈ 73 nm. The different nanoparticles sizes for these two series can be correlated with different ratio of Fe(acac)₃ and Zn(acac)₂ to the oleic acid and benzylether, used in the starting mixture.

The XRD patterns show the presence of only one phase, the inverse spinel cubic structure - Fig.2. The lattice parameters, listed in Table 1, are somewhat higher than those of pure magnetite. The increase in the lattice parameters, as compared with pure magnetite, suggests the

location of Zn²⁺ ions in tetrahedrally coordinated site, due to the larger ionic radius of Zn²⁺(0.74 nm) as compared with that of Fe³⁺ ions (0.49 nm) [15 - 17]. The elemental analysis by ICP-OES yielded a molar ratio Fe/Zn of 8.5±0.1 and 8.4±0.1, for series S1 and S2, respectively, with a 95% confidence level for the mean results and confidence interval. The mean sizes of the Zn doped nanoparticles, as determined from XRD measurements, are 30±1 nm (S1) and 50±1 nm (S2) in rather good agreement with the values obtained by TEM studies.

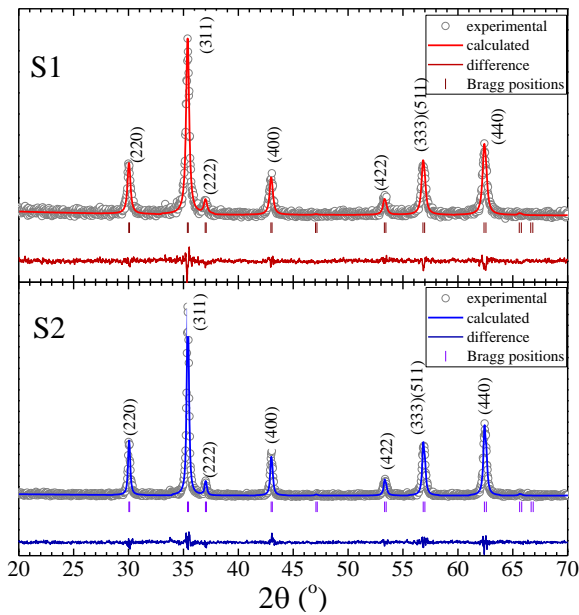


Fig. 2. XRD patterns at ambient temperature for samples S1 and S2 (color online)

Table 1. Lattice parameters and mean nanoparticles sizes

Sample	Lattice constants (nm)	Mean nanoparticles sizes (nm)	
		XRD	TEM
S1	0.841(3)	30±1	27
S2	0.840(9)	50±1	73

The magnetization isotherms, recorded at 5 K and 300 K, show that the saturation magnetizations are obtained in external fields of $\mu_0 H > 2$ T, for all samples, as shown in Fig. 3.

The saturation magnetizations are by $\approx 20\%$ higher than that of pure magnetite, in agreement with the location of Zn^{2+} ions in tetrahedral site. Starting from the formula unit $[Fe_{0.88}^{3+}Zn_{0.12}^{2+}]_A[Fe_{1.12}^{3+}Fe_{0.88}^{2+}]_B O_4$, and assuming ferrimagnetic type ordering, a magnetic moment of $\approx 4.72 \mu_B/f.u.$ is calculated, very close to those experimentally determined at $T = 5$ K, confirming the location of Zn^{2+} ions in tetrahedral sites - Table 2. The exchange interactions J_{ij} in magnetite are governed by a combination of antiferromagnetic superexchange (SE) and ferromagnetic double exchange (DE) interactions. As already pointed [18] ferrimagnetic ordering in Fe_3O_4 with high Curie temperature T_c , is obtained without any DE interaction when $J_{AB} \gg J_{BB}$, J_{AA} forming an antiparallel alignment of the moments on the A and B sites, respectively. When weakening the J_{AB} interactions, as result of substitutions at A sites and strengthening J_{BB} interactions, the B site magnetic moments cannot be parallelly orientated to the A site moments, leading to a canted magnetic structure [19, 20]. The replacement of iron by $x = 0.12$ Zn^{2+} ions, although decrease the Curie temperature, maintain the simplest ferrimagnetic ordering, where all iron moments are parallelly orientated, as confirmed by the result of magnetic measurements. This

trend was already evidenced for a zinc content up to $x \leq 0.2$ [19].

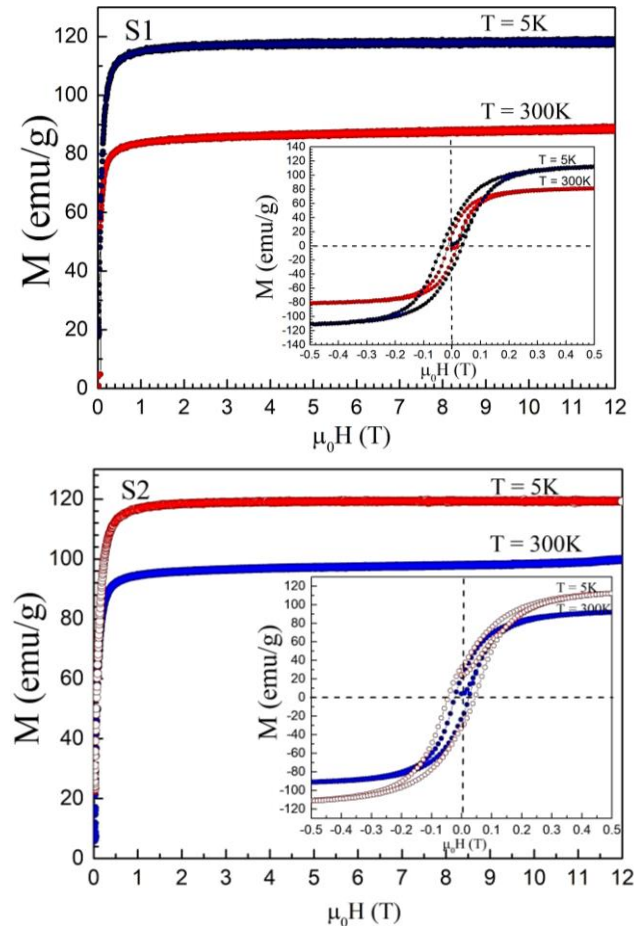


Fig. 3. Magnetization isotherms at $T = 5$ K and $T = 300$ K as well as the hysteresis loops (color online)

The hysteresis loops show the presence of small coercive fields at ambient temperature, $\mu_0 H_c = 0.01$ T (S1) and $\mu_0 H_c = 0.02$ T (S2), suggesting that the nanoparticles are close, to a superparamagnetic type behaviour at the above temperature. For S1 samples, the coercive field particularly seems to be due to the contribution of the nanoparticles fraction having sizes greater than 30 nm. The ratios between remanent (M_r) and saturation (M_s) magnetization at ambient temperature are approximately 0.10 for S1 and 0.22 for S2. These values are rather low and particle size dependent. These follow the general trend as evidenced in $Fe_{3-x}Zn_xO_4$ system; in spite of increasing the saturation magnetizations, with increasing Zn content, there is a decrease of M_r/M_s ratio [21].

The anisotropy constants were determined assuming that below the blocking temperature T_B , the anisotropy is uniaxial [22,23]. According to the Stoner-Wohlfarth model for noninteracting single domain particles, the coercivity, H_c , depends both on the anisotropy constant K as well as on saturation magnetization [24]:

$$H_c = \frac{2K}{\mu_0 M_s} \quad (1)$$

The determined anisotropy constants, according to the relation (1), at ambient temperature, are of $0.48 \cdot 10^4 \text{ J/m}^3$ (S2) and $0.22 \cdot 10^4 \text{ J/m}^3$ (S1), only little smaller than that of pure magnetite - Table 2. These values approximate the real anisotropy constants. In case of noninteracting

particles, a value of $M_r/M_s = 0.5$ is predicted, greater than those experimentally determined from hysteresis loops. The above trend can be explained assuming the presence of interactions between nanoparticles, influencing the estimated anisotropy constants.

Table 2. Magnetic properties

Sample	Saturation magnetization ($\mu_B/\text{f.u.}$)		Coercive field (T)		T_c (K)	T_B (K)	T_v (K)	Anisotropy constant $\text{K} \cdot 10^4 \text{ J/m}^3$		
	T=5K	T=300K	T=5K	T=300K				determined from H_c		determined from T_B
								T=5K	T=300K	T=300K
S1	4.91	3.95	0.04	0.01	756	400	26	1.2	0.48	0.23
S2	4.82	3.51	0.05	0.01	783	310	27	0.9	0.22	0.70

The temperature dependences of the ZFC and FC magnetization in the field of $\mu_0 H = 0.05 \text{ T}$ are given as example for S2 sample in Fig. 4.

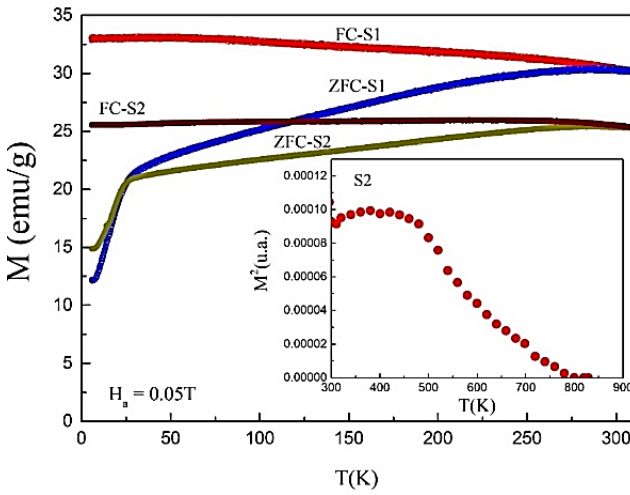


Fig. 4. Temperature dependences of the ZFC and FC magnetizations in the external field $\mu_0 H = 0.05 \text{ T}$ for the samples S1 and S2. In inset is shown the temperature dependence of the magnetization for the sample S2 (color online)

The separation point between the ZFC/FC curves corresponds to the maximum blocking temperature, T_s , whereas the peak position in the ZFC curve is related to the average blocking position, T_B [25]. The T_B value decreases parallelly with particle sizes. The maxima in the ZFC curves, located at T_B , define the temperature where the thermal energy becomes comparable to the anisotropy energy barrier and consequently it is related to the anisotropy constant:

$$T_B = \frac{K}{25k_B} V \quad (2)$$

where V is the nanoparticle volume and k_B is the Boltzmann constant. The anisotropy constants estimated from relation (2) are in the range of those obtained starting from coercive field, as shown in Table 2.

The magnetic particle's sizes or magnetic domain sizes, d_m , were estimated according to the relation [26]:

$$d_m = \left[\frac{18k_B T}{\pi} \frac{\chi_i}{\rho M_s^2} V \right]^{1/3} \quad (3)$$

By χ_i is denoted the initial susceptibility, ρ represents the sample density, and M_s is the saturation magnetization. Starting from the hysteresis loops at ambient temperature, the initial susceptibilities values were determined as 0.096 emu/gOe for sample S1 and 0.078 emu/gOe for sample S2. According to relation (3) the estimated domain sizes are $11 \pm 1 \text{ nm}$ for sample S1 and $9 \pm 1 \text{ nm}$ for sample S2. These values are smaller than the mean sizes of the nanoparticles determined from XRD and TEM investigations. Such differences were also shown in other reports and attributed to the approximation used in developing the model [27].

The ZFC magnetization curves evidence the presence of the Verwey transitions [10], at temperatures $T_v \approx 26 \text{ K}$ for both samples, not depending on particle sizes, as evidenced in Fig 4. In magnetite, the Verwey transition is not full-size dependent, like on nanoparticle shapes and morphology, being mainly influenced by the composition and stability of the nanoparticle surfaces [28]. Since the Verwey transition is caused by the phonon modes X_3 and Γ_5 which are linked to octahedral iron cations, the transition should be influenced by the dynamic and static positions of these ions [29]. Accordingly, a linear decrease of the Verwey transition temperature T_v with composition was observed in $\text{Fe}_{3-x}\text{Zn}_x\text{O}_4$ system in the composition range $0.01 \leq x \leq 0.04$, which can be described by the relation $T_v \approx 113-750x \text{ K}$. Considering the location of Zn^{2+} ions in tetrahedral sites, as well as the gradual change in the valence states of iron ions in the octahedral sites, we assumed that the T_v follows the same trend in our case. Thus, for the determined Zn content in our samples, of about $x \approx 0.12$, a Verwey temperature of 23 K is obtained using the above relation, nearly the same as the experimentally evidenced values. This suggests that the previously reported T_v trend evidenced for $x \leq 0.04$, is followed also for nanoparticles having higher Zn content, at least up to $x = 0.12$.

4. Conclusions

Octahedral shape $\text{Fe}_{2.88}\text{Zn}_{0.12}\text{O}_4$ nanoparticles with average sizes of 27 nm and 73 nm were successfully prepared by thermal decomposition. All samples crystallize in an inverse spinel cubic type structure with the Zn^{2+} ions located in tetrahedral sites. As result of the Zn^{2+} substitutions, the saturation magnetizations increase by $\approx 20\%$, while the estimated anisotropy constants are close to those of pure magnetite. The Verwey transition temperature T_V is not influenced by the nanoparticle sizes. The linear decrease of T_V values when increasing the Zn content can be correlated with the iron valence states in octahedral sites.

Acknowledgments

This work was supported by the Romanian Ministry of Education and Research (UEFISCDI), grant no. PN-III-P4-ID-PCCF-2016-0112 and through the research project to stimulate young independent teams (CNCSIS-UEFISCDI), grant no. PN-III-P1-1.1-TE-2016-096.

References

- [1] L. Gutiérrez, F. J. Lázaro, A. R. Abadía, M. S. Romero, C. Quintana, M. Puerto Morales, C. Patiño, R. Arranz, *Inorg. Biol.* **100**, 1790 (2006).
- [2] J. Wan, X. Jiang, H. Li, K. Chen, *J. Mater. Chem.* **22**, 13500 (2012).
- [3] M. Wen, Q. Li, Y. Li, *J. Electron Spectr. Related Phen.* **153**, 65 (2006).
- [4] B. Jeyadevan, K. Tohji, K. Nakatsuka, *J. Appl. Phys.* **76**, 6325 (1994).
- [5] S. A. Oliver, V. G. Harris, H. H. Hamdeh, J. C. Ho, *Appl. Phys. Lett.* **76**, 2761 (2000).
- [6] C. N. Chinnaamy, A. Narayanasamy, N. Ponpandian, K. Chattopadhyay, H. Guerault, J.-M. Greneche, *J. Phys. Cond. Matter.* **12**, 7795 (2001)
- [7] K. Tanaka, M. Makita, Y. Shimizugawa, K. Hirao, N. Soga, *J. Phys. Chem. Solids* **59**, 1611 (1998).
- [8] S. Nakashima, K. Fujita, K. Tanaka, K. Hirao, *J. Phys.: Condens. Matter.* **17**, 137 (2005).
- [9] A. Jha, N. Kumar, M. Sahni, A. Srivastava, Jyotirmay Dwivedi, Sanjay Chaubey, *J. Super. Novel Magn.* **31**, 107 (2018).
- [10] E. J. W. Verwey, E. L. Heilmann, *J. Chem. Phys.* **15**, 174 (1947).
- [11] S. Nakashima, K. Fujita, K. Tanaka, K. Hirao, T. Yamamoto, I. Tanaka, *Phys. Rev. B* **75**, 174443 (2007).
- [12] Y. Ma, J. Xia, C. Yao, F. Yang, S. G. Stanciu, P. Li, Y. Jin, T. Chen, J. Zheng, G. Chen, H. Yang, L. Luo, A. Wu, *Chem. Mater.* **31**, 7255 (2019).
- [13] H. M. Rietveld, *Journal of Applied Crystallography*, **2**, 65 (1969).
- [14] A. Mitra, J. Mohapatra, S. S. Meena, C. V. Tomy, M. Aslam, *J. Phys. Chem. C* **118**, 19356 (2014).
- [15] J. Takaobushi, H. Tanaka, T. Kawai, S. Ueda, J. J. Kim, M. Kobata, E. Ikenaga, Y. Nishino, D. Miwa, K. Tamasaku, T. Ishikawa, *Appl. Phys. Lett.* **89**, 242507 (2006).
- [16] B. D. Shannon, *Acta Cryst. A* **32**, 751 (1971).
- [17] N. Modaresi, R. Afzalzadeh, B. Aslibeiki, P. Kameli, A. Ghotbi Varzaneh, I. Orue, V. A. Chernenko, *J. Magn. Magn. Mater.* **482**, 206 (2019).
- [18] L. Néel, *Ass. Phys. (Paris)* **3**, 137 (1948).
- [19] Y. Yafet, C. Kittel, *Phys. Rev.* **87**, 290 (1952).
- [20] D. Venkateshvaran, M. Althammer, A. Nielsen, S. Geprägs, M. S. Ramachandra Rao, S. T. B. Goennenwein, M. Opel, R. Gross, *Phys. Rev. B* **79**, 134405 (2009).
- [21] S. Ueda, H. Tanaka, J. Takaobushi, E. Ikenaga, J. J. Kim, M. Kobata, T. Kawai, H. Osawa, N. Kawamura, M. Suzuki, K. Kobayashi, *Applied Phys. Express*, 077003 (2008).
- [22] D. Caruntu, G. Caruntu, C. J. O'Connor, *J. Phys. D: Appl. Phys.* **40**, 5801 (2007).
- [23] R. Dudric, G. Souca, Á. Szatmári, T. Szilárd, S. Nitica, C. Iacovita, A. I. Moldovan, R. Stiufluic, R. Tetean, E. Burzo, *AIP Conf. Proc.* **2218**, 030014 (2020).
- [24] E. C. Stoner, E. P. Wohlfarth, *Phil. Trans. Royal Soc. A* **240**, 599 (1948).
- [25] U. Voskoboynik, *Acta Phys. Pol. A* **92**, S-43 (1997).
- [26] E. E. Carpenter, *J. Magn. Magn. Mater.* **225**, 17 (2001).
- [27] K. O'Grady, A. Bradbury, *J. Magn. Magn. Mater.* **39**, 91 (1983)
- [28] M. Bohra, N. Agarwal, V. Singh, *J. Nanomater.* **2019**, Article ID 8457383 (2019).
- [29] Z. Kakol, D. Owoc, J. Przewoznik, M. Sikora, C. Kapusta, D. Zajac, A. Kolowski, J. E. Sabol, J. M. Honig, *J. Solid State Chem.* **192**, 120 (2012).

*Corresponding author: gabrielasouca@gmail.com